



Publication Year	2020
Acceptance in OA	2025-03-10T11:30:46Z
Title	Modeling MMS Observations at the Earth's Magnetopause with Hybrid Simulations of Alfvénic Turbulence
Authors	FRANCI, LUCA, STAWARZ, JULIA, PAPINI, EMANUELE, HELLINGER, PETR, NAKAMURA, TAKUMA, BURGESS, DAVID, Landi, Simone, VERDINI, ANDREA, MATTEINI, LORENZO, ERGUN, ROBERT
Publisher's version (DOI)	10.3847/1538-4357/ab9a47
Handle	http://hdl.handle.net/20.500.12386/36591
Journal	THE ASTROPHYSICAL JOURNAL
Volume	898



Modeling MMS Observations at the Earth’s Magnetopause with Hybrid Simulations of Alfvénic Turbulence

Luca Franci^{1,2} , Julia E. Stawarz³ , Emanuele Papini^{4,2} , Petr Hellinger^{5,6} , Takuma Nakamura⁷ , David Burgess¹ , Simone Landi^{4,2} , Andrea Verdini^{4,2} , Lorenzo Matteini³ , Robert Ergun⁸ , Olivier Le Contel⁹ , and Per-Arne Lindqvist¹⁰

¹ School of Physics and Astronomy, Queen Mary University of London, London, UK; l.franci@qmul.ac.uk

² INAF, Osservatorio Astrofisico di Arcetri, Firenze, Italy

³ Department of Physics, Imperial College London, London, UK

⁴ Dipartimento di Fisica e Astronomia, Università degli Studi di Firenze, Sesto Fiorentino, Italy

⁵ Institute of Atmospheric Physics, The Czech Academy of Sciences, Prague, Czech Republic

⁶ Astronomical Institute, The Czech Academy of Sciences, Prague, Czech Republic

⁷ Space Research Institute, Austrian Academy of Sciences, Graz, Austria

⁸ Laboratory of Atmospheric and Space Sciences, University of Colorado Boulder, Boulder, CO, USA

⁹ Laboratoire de Physique des Plasmas, CNRS/Ecole Polytechnique/Sorbonne Université/Université Paris-Saclay/Observatoire de Paris, Paris, France

¹⁰ KTH Royal Institute of Technology, SE-100 44 Stockholm, Sweden

Received 2019 November 15; revised 2020 May 30; accepted 2020 June 6; published 2020 August 5

Abstract

Magnetospheric Multiscale (MMS) observations of plasma turbulence generated by a Kelvin–Helmholtz (KH) event at the Earth’s magnetopause are compared with a high-resolution two-dimensional (2D) hybrid direct numerical simulation of decaying plasma turbulence driven by large-scale balanced Alfvénic fluctuations. The simulation, set up with four observation-driven physical parameters (ion and electron betas, turbulence strength, and injection scale), exhibits a quantitative agreement on the spectral, intermittency, and cascade-rate properties with in situ observations, despite the different driving mechanisms. Such agreement demonstrates a certain universality of the turbulent cascade from magnetohydrodynamic to sub-ion scales, whose properties are mainly determined by the selected parameters, also indicating that the KH instability-driven turbulence has a quasi-2D nature. The fact that our results are compatible with the validity of the Taylor hypothesis, in the whole range of scales investigated numerically, suggests that the fluctuations at sub-ion scales might have predominantly low frequencies. This would be consistent with a kinetic Alfvén wave-like nature and/or with the presence of quasi-static structures. Finally, the third-order structure function analysis indicates that the cascade rate of the turbulence generated by a KH event at the magnetopause is an order of magnitude larger than in the ambient magnetosheath.

Unified Astronomy Thesaurus concepts: [Plasma astrophysics \(1261\)](#); [Space plasmas \(1544\)](#); [Interplanetary turbulence \(830\)](#); [Astronomical simulations \(1857\)](#)

1. Introduction

Plasma turbulence is a fundamental phenomenon in many astrophysical systems, including the solar wind (e.g., Matthaeus & Velli 2011; Bruno & Carbone 2013; Kiyani et al. 2015; Chen 2016; Verscharen et al. 2019, and references therein) and the Earth’s magnetosphere (e.g., Vörös et al. 2006; Zimbardo et al. 2010; Breuillard et al. 2018; Macek et al. 2018; Pollock et al. 2018; Roberts et al. 2018), where it can be investigated by in situ spacecraft observations. It can be generated by different driving mechanisms, including plasma instabilities like the Kelvin–Helmholtz (KH) instability (KHI; e.g., Chandrasekhar 1961; Miura & Pritchett 1982). At the Earth’s magnetopause, this is driven by the velocity shear between the shocked solar wind and the magnetosphere and plays a fundamental role in their interaction (e.g., Mishin & Morozov 1983; Belmont & Chanteur 1989; Fairfield et al. 2000; Hasegawa et al. 2004; Foullon et al. 2008; Kivelson & Chen 2013; Nakamura 2020, and references therein). As a fluid/MHD instability, the KHI itself cannot directly mix the different plasmas from each side of the shear, as they remain frozen-in to the magnetic field. It can, however, be indirectly responsible for kinetic effects related to secondary

instabilities, e.g., Rayleigh–Taylor instability or magnetic reconnection (Faganello et al. 2008a, 2008b, 2014) or/and related to nonlinear regimes (vortex pairing) and to the formation of small-scale current sheets. These can account for transporting the solar wind into the magnetosphere and transferring energy, momentum, and particles across the sheared boundary layers.

Plasma turbulence has been studied for decades via theoretical modeling by direct numerical simulations (DNS), with different methods in different regimes and ranges of scales (e.g., Gary et al. 2012; Boldyrev et al. 2013; Karimabadi et al. 2013; TenBarge & Howes 2013; Vásconez et al. 2014; Vasquez et al. 2014; Franci et al. 2015a, 2015b; Parashar et al. 2015; Passot & Sulem 2015; Servidio et al. 2015; Told et al. 2015; Wan et al. 2015; Matthaeus et al. 2016; Cerri et al. 2017; Kobayashi et al. 2017; Passot et al. 2018; Pucci et al. 2017; Valentini et al. 2017; Grošelj et al. 2018; Arzamasskiy et al. 2019; Papini et al. 2019; Roytershteyn et al. 2019; Zhdankin et al. 2019). Both observations and DNS deliver spectra of the solar wind plasma and electromagnetic fluctuations exhibiting clear power laws over several decades in frequency (or, correspondingly, in wavenumber), with a transition (break) at the proton characteristic scales (e.g., Alexandrova et al. 2009; Sahraoui et al. 2009, 2010; Chen 2016). Such power-law behavior suggests that a turbulent cascade is at play at large fluid scales and continues all the way down to particle characteristic scales, where kinetic effects

become important. Despite a certain variability, mainly due to different plasma conditions, a general consensus has been achieved on the slope of different fields at scales larger and smaller than the ion-scale break, i.e., in the MHD/inertial and in the sub-ion range, respectively (e.g., Bale et al. 2005; Podesta et al. 2007; Alexandrova et al. 2009; Chandran et al. 2009; Sahraoui et al. 2010; Boldyrev et al. 2011; Chen et al. 2012, 2013; Šafránková et al. 2015, 2016; Chen 2016; Chen & Boldyrev 2017; Matteini et al. 2017).

The cascade is characterized by intermittency (e.g., Matthaeus et al. 2015), expressed by non-Gaussian probability distribution functions (PDFs) of the turbulent fluctuations, due to the presence of discontinuities and current sheets at different scales. Such departure from a normal distribution is observed to increase as smaller scales are approached, likely due to the presence of ion-scale current sheets and magnetic reconnection sites (e.g., Bruno 2019, and references therein).

Theoretical predictions for the turbulent cascade rate can be obtained by assuming incompressibility, homogeneity, and isotropy. These derive from a law that links the cascade/dissipation rate to third-order mixed structure functions involving magnetic and velocity fluctuations (de Kármán & Howarth 1938; Politano & Pouquet 1998). Such a relation is observed as a linear scaling of the structure functions with the separation scale in the inertial range (MacBride et al. 2005; Sorriso-Valvo et al. 2007; Verdini et al. 2015), where the cascade rate represents the coefficient (apart from a factor $-4/3$). Recently, more realistic versions of this law have also included the effects of compressibility (Andrés et al. 2018; Hadid et al. 2018; Hellinger et al. 2020).

Although spacecraft observations represent unique opportunities to measure in situ plasma properties, they provide only single-point or, at most, few-point measurements, performed at specific moments in time. Often, they are not equipped to measure all fields simultaneously and/or they do so with different time resolutions. DNS provide fundamental complementary information, e.g., particle distribution functions and their moments and electromagnetic fields at many millions of grid points simultaneously, with the same spatial and time resolution, accompanied by two-dimensional (2D) and/or three-dimensional (3D) images. Thanks to the recently increased accuracy in both spacecraft measurements and DNS, we can now fully exploit their synergy by reproducing and interpreting observations with numerical modeling. This allows us to probe the plasma dynamics down to scales shorter than the ion characteristic scales, which we will refer to as “sub-ion scales” or more generally as “kinetic scales,” since it is there that the ion kinetic effects might start to play a role in the plasma dynamics.

Here, we compare a high-resolution 2D hybrid (particle-in-cell protons, mass-less fluid electrons) DNS of decaying Alfvénic turbulence (see Franci et al. 2015a) with Magnetospheric Multiscale (MMS) observations of plasma turbulence generated by a KH event at the Earth’s magnetopause (Stawarz et al. 2016). Unlike in observations and previous DNS of KH-driven turbulence (e.g., Nakamura et al. 2011, 2013), here the large-scale energy injection is not due to a super-Alfvénic vortex flow. We investigate numerically the development of the turbulent cascade after the initial injection has occurred by setting the ion and electron plasma betas, the turbulence strength, and the injection scale to their observational values, to mimic the observed plasma conditions.

The paper is organized as follows. In Section 2, we describe how the observational and numerical data sets have been selected and post-processed. In Section 3, we compare the MMS and DNS results, with particular focus on the power spectra of electromagnetic and plasma fluctuations (Section 3.1), intermittency (Section 3.2), and cascade rate (Section 3.3). Finally, in Section 4, we discuss and summarize our findings and their physical implications.

2. Data Sets

2.1. Observational Data Set

The observational data set consists of 54 subintervals of high-resolution “burst” data collected by MMS on the duskside magnetopause on 2015 September 8 over a ~ 1.5 hr long interval in which a continuous train of KH waves were observed. Such subintervals are the same as those examined by Stawarz et al. (2016) and were manually selected such that they were all located within individual KH vortices. The statistics (e.g., spectra) presented in this study are taken to be the ensemble average based on these 54 intervals. This choice allows us to investigate the properties of the turbulent plasma avoiding the periodic compressed current sheets associated with the large-scale KH wave, which would skew the statistics if included in the analysis. As a consequence of such selection, the power spectra (see Section 3.1) represent the ensemble average of turbulent fluctuations inside each of the vortices and no enhancement in the power corresponding to the scale of the KH vortices is expected to be present at the examined frequencies. In this KH event, the magnetosheath magnetic field is northward and the field strength is nearly constant across the magnetopause. The “guide field” is taken to be the average field $B_0 = \langle B \rangle$ within each subinterval. The magnetic field is dominated by the B_{zGSE} component and so the perpendicular plane associated with the turbulence is nearly the $x_{GSE}-y_{GSE}$ plane.

The data set contains magnetic field measurements from the fluxgate (Russell et al. 2016) and the search coil (Le Contel et al. 2016) magnetometers at 1/128 and 1/8192 s cadences respectively, electric field measurements from the electric field double probes (Ergun et al. 2016; Lindqvist et al. 2016) at 1/8192 s cadence, and ion and electron particle moments, as measured by the fast plasma investigation (Pollock et al. 2016), at 0.15 and 0.03 s cadences respectively. Prior to averaging, the magnetic field was normalized to B_0 , the electric field to $B_0 V_A$, the ion and electron bulk velocities to V_A , and the electron density to n_0 , where the Alfvén velocity, V_A , and the background density, n_0 , are defined based on average parameters from each subinterval.

Aspects of this KH event, including magnetic reconnection (Eriksson et al. 2016a, 2016b; Li et al. 2016; Vernisse et al. 2016; Sturmer et al. 2018), turbulence (Stawarz et al. 2016; Sorriso-Valvo et al. 2019), waves (Wilder et al. 2016), and mass transport (Nakamura et al. 2017a, 2017b) properties, have been examined in a number of previous studies. Eriksson et al. (2016a) provide an overview of the properties of the overall KHI within this event, which is characterized by an average ion inertial length of $d_i \sim 65$ km and a KH wavelength of the order of $300 d_i$.

2.2. Numerical Data Set

The numerical data set was obtained from a high-resolution 2D DNS of plasma turbulence performed with the hybrid (particle-in-cell ions and mass-less fluid electrons) code CAMELIA (Franci et al. 2018a). The temporal and spatial units are the inverse ion gyrofrequency, Ω_i^{-1} , and the ion inertial length, d_i . The magnetic field is expressed in units of the magnitude of the ambient magnetic field, B_0 , the ion bulk velocity in units of the Alfvén velocity, V_A , and the ion density in units of the background density, n_0 , as for the respective observational quantities. The initial conditions are the same as those in Franci et al. (2015a, 2015b). These consist of a homogeneous plasma in the (x, y) simulation plane, embedded in a uniform out-of-plane ambient magnetic field, $\mathbf{B}_0 = B_0 \hat{z}$. The simulation plane corresponds to the plane perpendicular to \mathbf{B}_0 in the observations, which is nearly the $x_{\text{GSE}}-y_{\text{GSE}}$ plane, as noted above. The plasma is perturbed by in-plane balanced Alfvénic fluctuations, i.e., magnetic and ion bulk velocity fluctuations with zero mean cross helicity. These are the superposition of modes with the same amplitude and random phases in the range $-0.2 \leq k_{x,y} d_i \leq 0.2$, so that $k_{\perp}^{\text{max}} d_i \sim 0.3$, which we will refer to as the “injection scale.” The parallel wavevector with respect to \mathbf{B}_0 is by construction $k_{\parallel} = 0$, so that $\mathbf{k} \equiv \mathbf{k}_{\perp}$. This, however, still allows for parallel propagation with respect to the local mean field, as a consequence of the bending of the magnetic field lines due to the in-plane magnetic fluctuations. Our initialization does not intend to be representative of the real environment explored by MMS since the KHI, which is the driving mechanism of the observed turbulence, is not included in our DNS. We do, however, reproduce similar plasma conditions by setting the following physical parameters accordingly to their observational values: ion beta $\beta_i = 0.42$, electron beta $\beta_e = 0.065$, amplitude of the initial fluctuations $\mathbf{B}^{\text{rms}}/B_0 \sim 0.14$, and injection scale $k_{\perp}^{\text{max}} d_i \sim 0.3$. The numerical parameters are 16384 particle-per-cell (ppc), 4096×4096 grid points, box size $L_x = L_y = 256 d_i$ (of the same order of the KH wavelength for the observed event, see above), spatial resolution $\Delta x = \Delta y = d_i/16$, time resolution $\Delta t = 0.01 \Omega_i^{-1}$ for the particle advance and $\Delta t_B = \Delta t/10$ for the magnetic field advance, and resistivity $\eta = 2 \times 10^{-4} 4\pi V_A c^{-1} \Omega_i^{-1}$. The optimal value for η has been chosen empirically, based on our previous simulations with similar parameters. This prevents an accumulation of the energy in magnetic fluctuations at small scales due to numerical noise and assures a satisfactory conservation of the total energy (Franci et al. 2015a). The development of the turbulent cascade is qualitatively the same as in Franci et al. (2017). The simulation has been run until $350 \Omega_i^{-1}$, when the rms value of the current density has reached a plateau. At this time, a turbulent quasi-stationary state has been achieved, characterized by magnetic field structures at all scales (Figure 1(a)) and small-scale current structures between vortices (Figure 1(b)). We perform our analysis at $300 \Omega_i^{-1}$, without performing any time average. We have verified that spectra and other properties do not change significantly between that time and the end of the simulation.

3. Results

3.1. Spectral Properties

The observational and numerical spectral properties of the electromagnetic and plasma fluctuations are shown in Figures 2 and 3, respectively, using red dashed-dotted lines for MMS and black solid ones for the DNS. Four vertical dashed lines mark

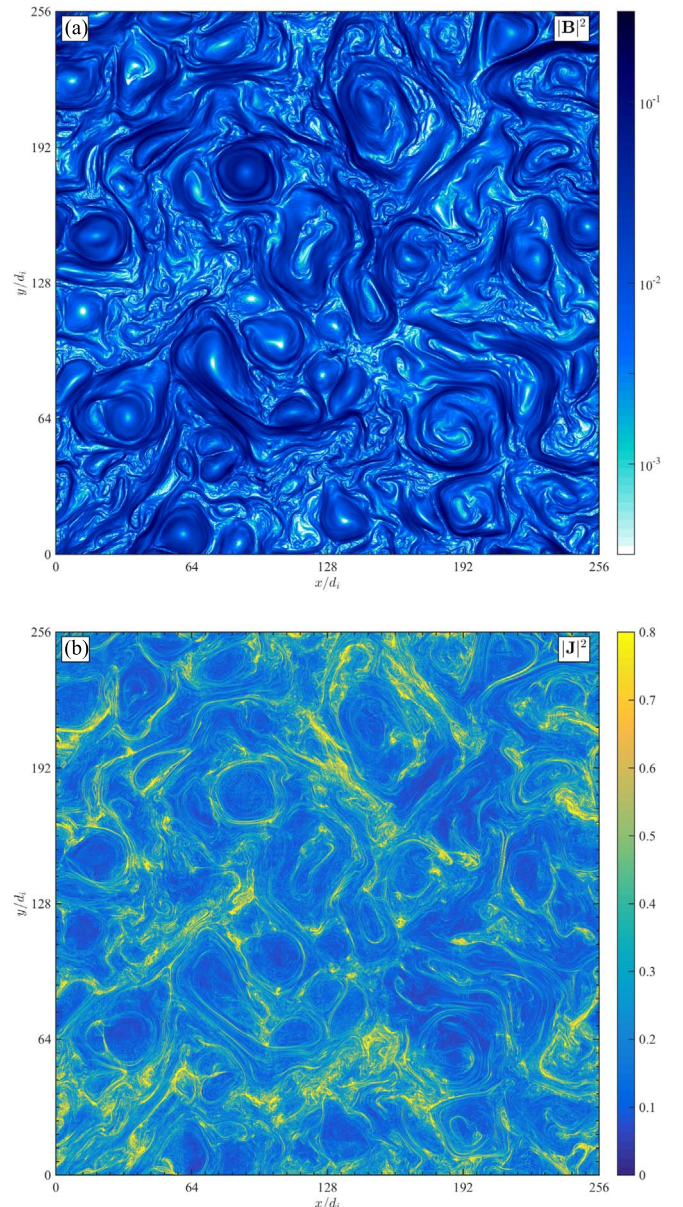


Figure 1. Contour plots of the magnitude of the magnetic fluctuations (a) and of the current density (b) in the whole DNS domain at the final time.

the particle characteristic scales, i.e., from small to large wavenumbers, the ion inertial length, d_i , the ion gyroradius, $\rho_i = \sqrt{\beta_i} d_i$, the electron inertial length, d_e , and the electron gyroradius, $\rho_e = \sqrt{\beta_e} d_e$. In the top panels, the 1D power spectra of each field are compared. The MMS spectra have been converted from frequency, f , to perpendicular wavenumber with respect to the ambient magnetic field, k_{\perp} , using the “frozen flow” Taylor hypothesis (Taylor 1938). Under the assumptions that the average perpendicular ion bulk flow velocity computed over the 54 subintervals, $U_{0,\perp} = 170 \text{ km s}^{-1}$, is much larger than its parallel counterpart, $U_{0,\parallel} = 33 \text{ km s}^{-1}$ (Stawarz et al. 2016) and that $k_{\perp} \gg k_{\parallel}$ (consistent with Alfvénic turbulence), such a hypothesis yields $k_{\perp} = 2\pi f/U_{0,\perp}$ (Bourouaine et al. 2012). The difference between this estimate of k_{\perp} and the longitudinal wavenumber estimated as $2\pi f/U_0$ is here only 2%, indicating that the spacecraft is essentially sampling k_{\perp} as the plasma flows past it. Therefore, in the remaining analysis we will utilize the

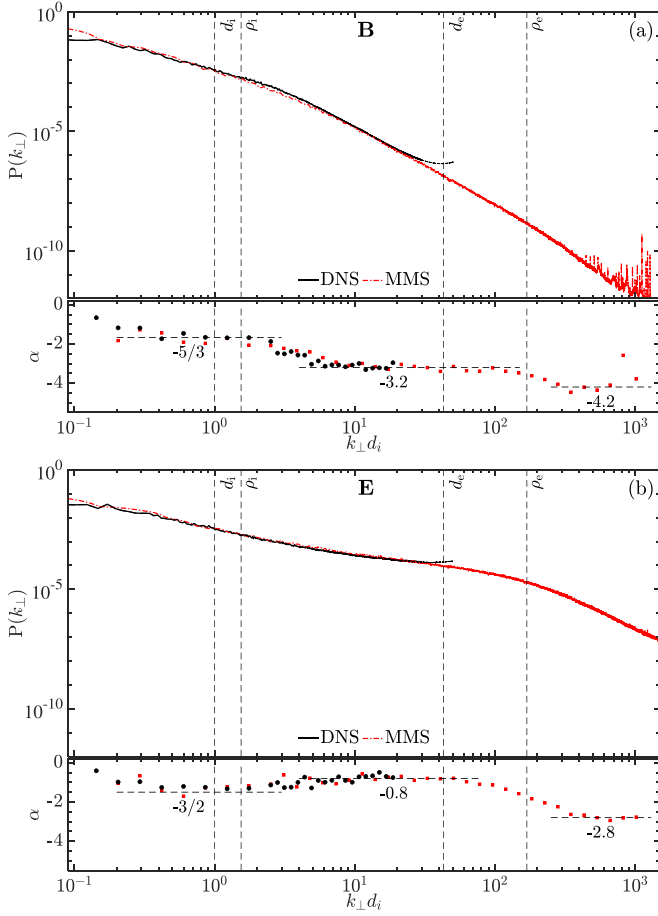


Figure 2. Spectral properties of the electromagnetic fluctuations: magnetic field (a) and electric field (b). Upper panels: 1D MMS and DNS spectra. Bottom panels: local slope, α .

estimate of k_{\perp} obtained under the assumption that $k_{\perp} \gg k_{\parallel}$, as this is the component of the wavevector most compatible with the DNS. The DNS spectra have not been rescaled in amplitude and their portions affected by numerical noise are drawn as dotted lines. In the bottom panels we compare the values of the local spectral index, α , obtained by performing many power-law fits on small intervals in k_{\perp} . For each field, horizontal power laws with characteristic slopes are drawn as a reference.

In Figure 2(a), we analyze the fluctuations of the magnetic field, \mathbf{B} . The MMS spectrum exhibits a triple power-law-like behavior over four decades in wavenumber, with a first steepening around the ion scales and a second one around the electron scales. It is closely followed by the DNS spectrum over two full decades where the numerical noise is negligible, i.e., in the wavenumber interval $0.3 \lesssim k_{\perp} d_i \lesssim 30$. The bottom panel shows that the first power-law slope is compatible with the $-5/3$ prediction for the inertial-range turbulent cascade (Goldreich & Sridhar 1995). A transition is observed in correspondence of $k_{\perp} d_i \sim 3$, consistently with previous DNS with a similar plasma beta (Franci et al. 2015a, 2015b, 2016). A second, steeper ($\alpha \sim -3.2$), power law is observed at sub-ion scales, extended for over a decade and a half in MMS, up to $k_{\perp} d_i \sim 100$, and over slightly less than a decade in the DNS, until the resolution limit is reached. A second transition is observed in the data just before the electron scales are met, followed by a third, much narrower interval where the instrumental noise becomes

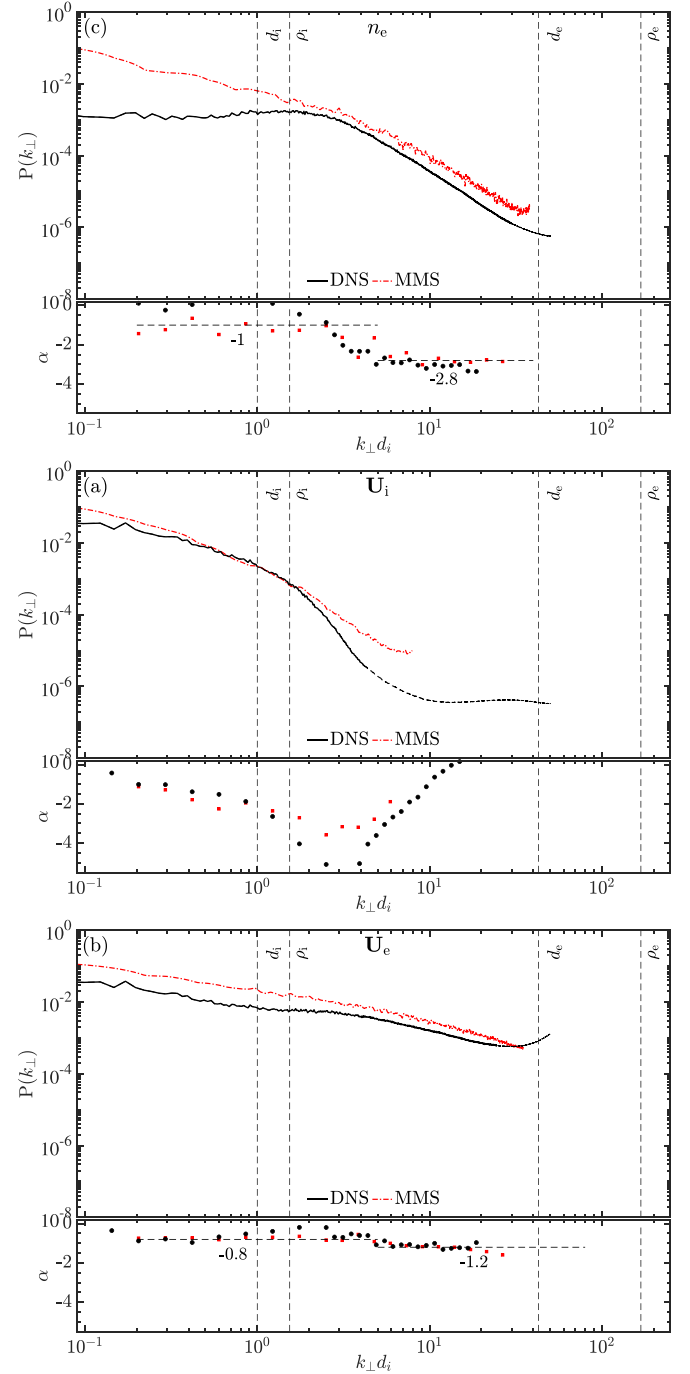


Figure 3. Same as in Figure 2 (but with different vertical and horizontal scales), for the plasma fluctuations: electron density (a) as well as ion (b) and electron (c) velocity.

important, so that no clear power law can be inferred, despite a hint of a further steepening.

Three distinct, clearer, power-law intervals are observed in the MMS spectrum of the electric field, \mathbf{E} (Figure 2(b)). The agreement with the DNS spectrum is particularly remarkable, since in the hybrid model \mathbf{E} is computed from the generalized Ohm's law involving the other fields and their derivatives, so it is more sensitive to both physical parameters (e.g., ion and electron beta) and small-scale numerical noise (e.g., from the density and the current density). The first interval is compatible with a power law with slope $-3/2$, followed by a flattening

to ~ -0.8 at sub-ion scales. Both these spectral indices are consistent with theoretical predictions from the generalized Ohm's law (Franci et al. 2015a). In correspondence with the electron scales, the MMS spectrum shows a second transition and a steepening, hinting at a third power-law interval with slope ~ -2.8 , although less extended than a decade, for $300 \lesssim k_{\perp} d_i \lesssim 1000$.

The spectral properties of the density fluctuations are compared in Figure 3(a). MMS measures both the ion, n_i , and the electron density fluctuations, n_e , with two different instruments and resolutions. In the hybrid model, since the electrons are treated as a mass-less fluid, these two quantities are assumed to be the same. Therefore, here we only show the observed electron density, which has a higher time resolution, corresponding to the DNS spatial resolution. In the inertial range, the MMS and DNS density fluctuations exhibit a very different spectral behavior, due to the fact that the latter is initialized with no density fluctuations and this keeps the large-scale compressibility lower. The MMS spectrum exhibits a power-law behavior with a slope compatible with -1, consistent with previous spacecraft observation in the solar wind (Šafránková et al. 2015). At ion and sub-ion scales, a small difference in the level of fluctuations between MMS and the DNS is observed, of the same order of the one observed for the electron velocity spectra. Nevertheless, a good agreement is recovered for the slope below the ion scales, which is consistent with -2.8 . This confirms that the level of compressibility in the inertial range does not impact significantly the nature of the fluctuations in the kinetic range (Cerri et al. 2017). The shape of the MMS spectrum of n_i (not shown) is the same as for n_e in the whole range of resolved scales: the slope is the same, i.e., ~ -1 at large scales and ~ -2.8 at small scales, while the level of fluctuations is slightly lower, likely due to the MMS FPI density estimates, and in better agreement with, but still slightly overestimating, the DNS spectrum at sub-ion scales.

The spectra of the ion bulk velocity, U_i (Figure 3(b)), show no clear extended power-law interval in either the inertial range or the kinetic one. The level of the ion bulk velocity fluctuations strongly drops at $k_{\perp} d_i \sim 1$, so there is not even a full decade separating the break from the injection scale. Approaching the kinetic scales, both the MMS and the DNS spectra flatten due to instrumental and numerical noise, respectively. In the range of scales not affected by noise, the two spectra are still in quite good qualitative agreement.

Figure 3(c) compares the MMS and DNS spectra of the electron bulk velocity, which in the hybrid model is computed as $U_e = U_i - (\nabla \times \mathbf{B})/n$. By chance, the maximum wavenumber is the same, since the spatial resolution of the DNS corresponds to the observational time resolution for this field. A small discrepancy in the level of fluctuations is observed over the whole range of scales, whose origin is not clear. The DNS spectrum of U_e in the kinetic range is just that of \mathbf{B} multiplied by k_{\perp}^2 , consistently with the fact that the ion bulk velocity fluctuations are negligible at those scales and so the current is almost entirely supported by the electron bulk motion, i.e., $\nabla \times \mathbf{B} = \mathbf{J} = n_i \mathbf{U}_i - n_e \mathbf{U}_e \sim -n \mathbf{U}_e$. Despite the slightly different level, the slope of the two spectra of U_e is almost exactly the same at all scales. The only difference is a small flattening in the DNS spectrum around the ion scales, which brings the level of fluctuations at kinetic scales slightly

closer to the observational one. This can be seen as a small bump in the value of the local slope, visible in the bottom panel, between the scale corresponding to d_i and the scale of the break in the magnetic field spectrum.

The slopes of the different fields in the sub-ion range, i.e., $3 \lesssim k_{\perp} d_i \lesssim 40$, are not all independent. The one of the electric field, $\alpha_E \sim -0.8$, is related to the one of the density and of the parallel magnetic fluctuations (not shown), $\alpha_n \sim \alpha_{B_{\parallel}} \sim -2.8$, by the simple relation $\alpha_E \sim \alpha_{n(B_{\parallel})} - 2$. This comes from the electron pressure gradient term and the Hall term in the generalized Ohm's law, the latter being dominated by its first-order contribution $(\nabla \times \mathbf{B}_{\parallel}) \times \mathbf{B}_0$ (Franci et al. 2015a). The kinetic-scale slope of the electron bulk velocity spectrum is instead related to the one of the perpendicular magnetic fluctuations (not shown, but similar to the total magnetic field, representing its dominant contribution), $\alpha_{B_{\perp}} \sim -3.2$, according to $\alpha_{U_e} \sim \alpha_{B_{\perp}} + 2$. This is due to the fact that the out-of-plane current density is much larger than its in-plane component and the ion bulk velocity drops at ion scales, so $\mathbf{J} \sim \mathbf{J}_{\parallel} \sim \nabla \times \mathbf{B}_{\perp} \sim n_0 \mathbf{U}_e$.

3.2. Intermittency

The intermittency properties are compared in Figure 4, showing the PDFs of the in-plane increments of a magnetic field component perpendicular to \mathbf{B}_0 , $\delta B_y(k_{\perp})/\delta B_{y,\text{rms}}$. Six different values of $k_{\perp} d_i$ are explored, representing the inertial range, $k_{\perp} d_i = 0.6$ (panel (a)) and 1.2 (b), the ion-scale transition, $k_{\perp} d_i = 2.4$ (c) and 2.33 (f), and the ion kinetic range, $k_{\perp} d_i = 4.8$ (d) and 9.6 (e). For the DNS (black curves), these are simply obtained from $k_{\perp} = 2\pi/\ell$, where ℓ is the spatial lag in the simulation plane. For MMS (red curves), this only holds for panel (f), where the increments are actually computed from the spatial lag, while for (a)–(e) the temporal lag, τ , has been converted to the corresponding wavenumber using the Taylor hypothesis.

The PDFs of magnetic fluctuations present very different shapes at different scales. At scales close to the injection scale, it is quite similar to a Gaussian distribution (dotted black curve), deviating from it only in correspondence of the largest fluctuations. The PDFs become less and less Gaussian toward smaller lags, developing extended tails at kinetic scales. For fluctuations with an amplitude smaller than 4 times the rms value, $\delta B_y(k_{\perp}) < 4 \delta B_{y,\text{rms}}$, the numerical and observational PDFs are almost overlapped at all scales, apart from small differences in the kinetic range. In the tails, the PDFs from the DNS are usually higher than their observational counterpart (such differences are almost negligible if we consider that there the number of counts is small and concentrated in very few points in the simulation domain). Such intermittency properties are consistent with the excess kurtosis, shown in Figure 5. Both the DNS (black) and the MMS (red) kurtosis are very small at large scales, down to $k_{\perp} d_i \sim 1$. They increase in the kinetic range, with a similar but still different trend, such that their values at $k_{\perp} d_i \sim 10$ differ by a factor of ~ 2 . The DNS kurtosis is seen to be very sensitive to the tails of the PDFs, where the results suffer from resolution effects. Moreover, at earlier times, it assumes larger values by about 2 orders of magnitude, peaking at more than 100 in correspondence with the onset of magnetic reconnection, when strong current sheets are just about to start being disrupted.

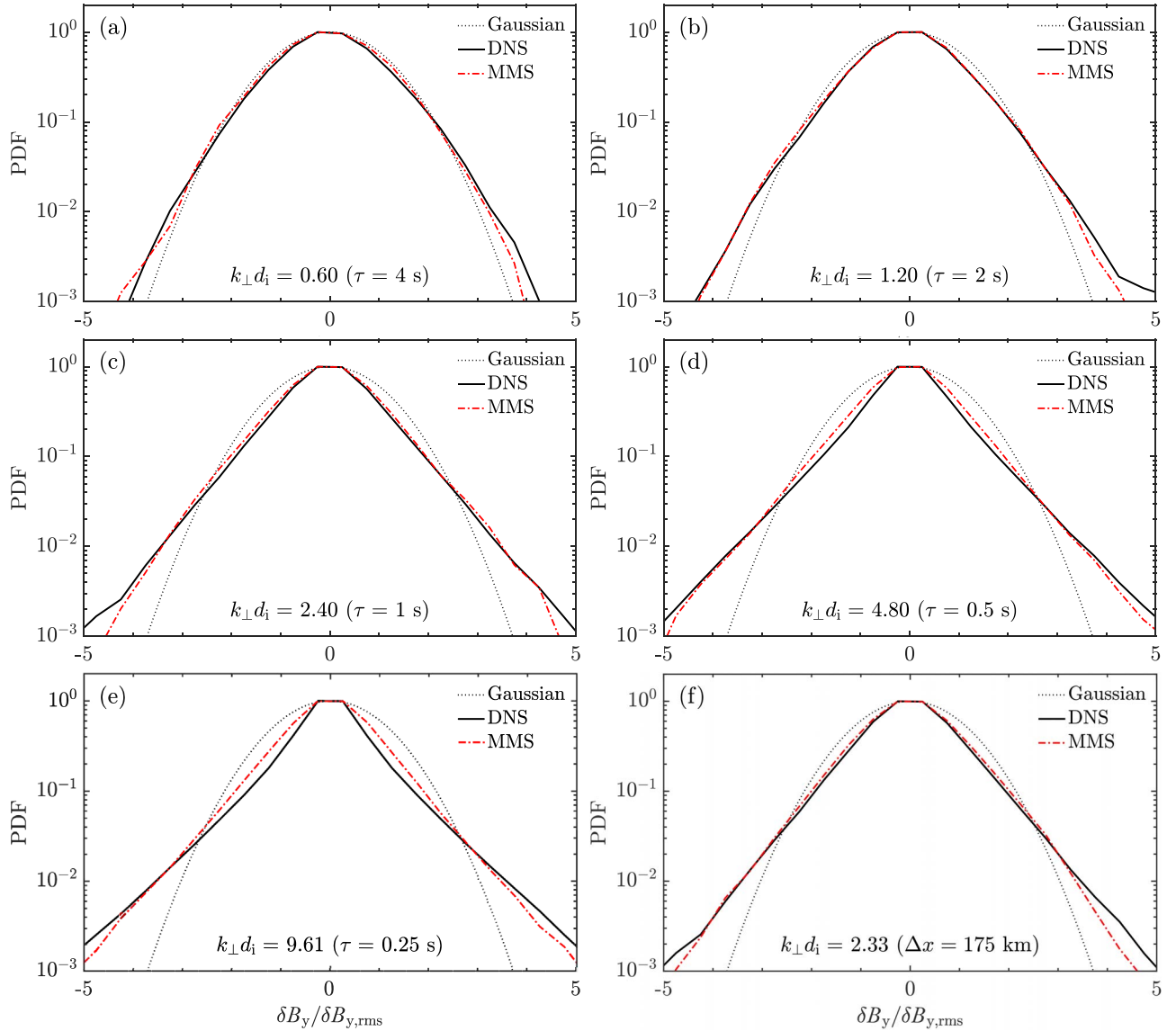


Figure 4. (a)–(e) Normalized probability distribution functions of magnetic field increments at different wavenumbers, corresponding to different temporal lags. (f) The same as in the previous panels, for a spatial lag $\Delta x \approx 175$ km (corresponding to the MMS formation size).

3.3. Cascade Rate

The cascade rate properties can be investigated by using the statistical von Kármán–Howarth/Politano–Pouquet law (de Kármán & Howarth 1938; Politano & Pouquet 1998) for the mixed third-order structure function

$$Y = \langle \delta U |\delta U|^2 + \delta U |\delta \mathbf{b}|^2 - 2\delta \mathbf{b} (\delta U \cdot \delta \mathbf{b}) \rangle, \quad (1)$$

where the increments of the bulk velocity, δU , and of the magnetic field in Alfvénic units, $\delta \mathbf{b}$, are computed between two points x and $x + l$ and $\langle \rangle$ denotes the average over x . This law predicts for the MHD inertial range a linear scaling of Y_L with the separation scale l , where Y_L is longitudinal component. Figure 6 compares $-Y_L/l$ as a function of l from MMS and the DNS. Both curves exhibit a similar profile with a plateau, but they do not show a clear linear scaling of Y_L (or a constant value of $-Y_L/l$), a signature of the inertial range. This is likely due to the fact that the energy injection takes place at scales not

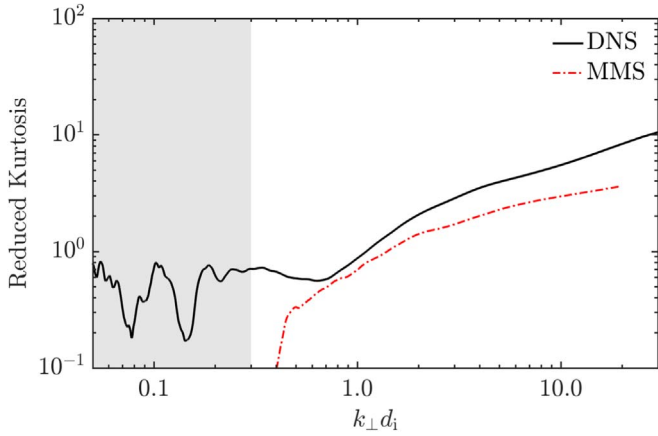


Figure 5. Excess kurtosis of magnetic field increments. The gray shaded area marks the range of scales where energy is initially injected in the DNS.

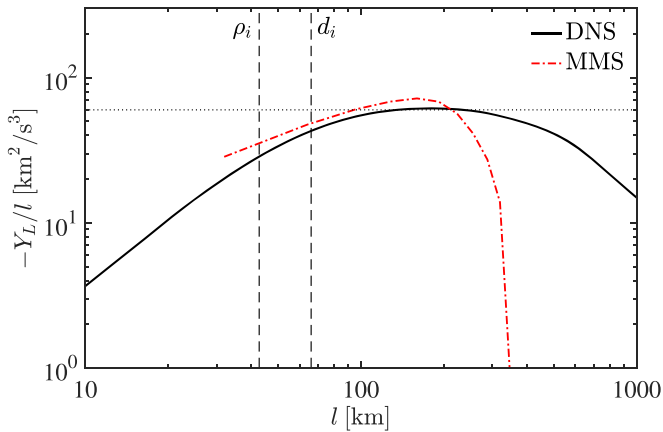


Figure 6. MHD structure function from generalized third-order law, $-Y_L$, divided by the spatial lag, l , vs. l in km.

far enough from the ion ones and in the sub-ion range the Hall physics must be included (Papini et al. 2019). Indeed, recent simulations and observations indicate that the turbulent energy cascade partly continues via the Hall term (Hellinger et al. 2018; Bandyopadhyay et al. 2020). Figure 6, however, shows that MMS and the DNS exhibit very similar values (for the separation length in the range between about 50–200 km). Assuming isotropy, we get (at the plateau) a cascade rate of $\sim 5 \times 10^7 \text{ J kg}^{-1} \text{ s}^{-1}$, a value about 10 times larger than the one observed in the Earth’s magnetosheath (Bandyopadhyay et al. 2018; Hadid et al. 2018).

4. Conclusions and Discussion

We have reproduced MMS observations of KH-generated turbulence at the Earth’s magnetopause with a high-resolution 2D hybrid DNS of Alfvénic plasma turbulence. We have used the observed values of four fundamental physical parameters that determine the plasma conditions (ion and electron beta, turbulence strength, and injection scale). No other free parameters have had to be used to optimize the agreement.

The MMS and DNS spectra of the electromagnetic fluctuations exhibit an unprecedented quantitative agreement. The ion beta controls the scale and shape of the ion-scale spectral break in the magnetic field (Franci et al. 2016), while the electron beta affects the level of the electron-pressure-gradient term in the generalized Ohm’s law (Franci et al. 2015a; Matteini et al. 2017), determining the level of electric field fluctuations in the inertial range. Although the level of ion and electron bulk velocity and density fluctuations is slightly different, the spectral indices are very similar. The only major difference is the level of compressibility at MHD scales, lower in the DNS due to the initial conditions.

The agreement between MMS observations and the DNS extends to intermittency. In both cases the PDFs of magnetic fluctuations in the inertial range are very close to a Gaussian distribution and, consequently, the excess kurtosis is close to zero, rapidly increasing monotonically toward smaller scales. At both extremes of the range of scales here investigated, the intermittency properties differ from what is typically observed in the solar wind, where the kurtosis is larger at MHD scales and exhibits a plateau or a decrease at sub-ion scales (e.g., Kiyani et al. 2009, 2013; Wu et al. 2013; Chen et al. 2014; Chen 2016; Chhiber et al. 2018). The former discrepancy is

related to the fact that the injection scale here is just about one order of magnitude larger than the ion scales, so that MHD-scale current sheets are unlikely to form and only vortices (and, possibly, wave-like fluctuations) are present in the inertial range. The origin of the different behavior at sub-ion scales is not trivial. It could be related to a larger presence of proton and electron-scale current sheets in the magnetosheath with respect to the solar wind, as shown in Chhiber et al. (2018), possibly as the consequence of the continuous formation of KH vortices interacting with each other. This topic will be further discussed in a following paper.

The behavior of the mixed third-order structure function is consistent with the picture above: both the MMS and the DNS inertial ranges are quite small and a change in the nature of the fluctuations is observed at ion scales. This is where the MHD approximation of the third-order exact law stops to hold and Hall and kinetic effects need to be taken into account to have a comprehensive estimate of the cascade rate. The KHI-driven turbulence is observed to be much stronger than what is typically observed for ambient magnetosheath turbulence, since its cascade rate is an order of magnitude larger. Our DNS recovers a comparable value. The key parameter that allows for such a quantitative agreement is the use of the MMS-observed amplitude of magnetic fluctuations in our DNS. The fact that this cascade rate is larger than the one observed in the Earth’s magnetosheath (by about an order of magnitude; Bandyopadhyay et al. 2018; Hadid et al. 2018) is consistent with the turbulence being driven by the KHI instead of just preexisting background turbulence. It is important to recall that the von Kármán–Howarth/Politano–Pouquet law that we employ to estimate the cascade rates is exact only under the assumption of incompressible (MHD) turbulence. The use of a more realistic compressible law (Andrés et al. 2018; Hadid et al. 2018; Hellinger et al. 2020) may lead to even larger cascade rates than the ones presented here.

The overall quantitative agreement between MMS observations and our DNS confirms that the hybrid approach is optimal for investigating the properties of the turbulent cascade simultaneously from MHD down to sub-ion scales, provided that a high accuracy is employed. All the main physical processes seem to be included and correctly reproduced in the model and the ones missing are likely not fundamental in the plasma dynamics at these scales and in these plasma conditions. As a consequence, as far as the spectral and intermittency properties are concerned, they represent a preferable choice in those situations where the cascade needs to be followed over a wide range of scales simultaneously and/or with a very high accuracy at kinetic scales.

This work further confirms the quasi-2D nature of plasma turbulence in the presence of a strong guide field, with the cascade mainly developing in the perpendicular direction, as suggested by 3D DNS employing different methods (e.g., Cerri et al. 2019, and references therein) and by a direct quantitative comparison between 2D and 3D CAMELIA DNS (Franci et al. 2018a, 2018b).

The agreement between our numerical results and the observational results converted from frequencies to wavenumbers is compatible with the validity of the Taylor hypothesis at the magnetopause down to sub-ion scales (Chen & Boldyrev 2017; Chhiber et al. 2019; Stawarz et al. 2019). This would imply that the fluctuations at sub-ion scales are predominantly low-frequency,

consistent with quasi-static structures or with a Kinetic Alfvén wave-like nature (Hasegawa et al. 2020).

Interestingly, in both the KH event and in the DNS a strong interplay between turbulence and magnetic reconnection is observed. At the magnetopause, reconnection occurs in intense current sheets forming at the trailing edges of KH-related surface waves and turbulence develops in the reconnection exhausts (Eriksson et al. 2016a). In the DNS, reconnection is driven by the interaction of large-scale vortices and it is observed to act as a driver for the development of the kinetic-scale cascade (Franci et al. 2017; Papini et al. 2019). Since the properties of turbulence and reconnection, as well as their interplay, are likely controlled by the plasma conditions (including the injection scale), rather than by the nature of the injection mechanism, the role of reconnection observed in both the KH event and in the DNS could provide a possible explanation for the agreement. Indeed, there is evidence that the correlation length of the turbulence can change how reconnection proceeds (i.e., electron-only reconnection; Phan et al. 2018; Sharma Pyakurel et al. 2019; Stawarz et al. 2019).

Summarizing, the physical implications of the direct comparison between MMS observations and our 2D DNS of decaying balanced Alfvénic turbulence are:

- (i) KHI-driven turbulence at the magnetopause has spectral and intermittency properties compatible with balanced Alfvénic turbulence from MHD scales down to sub-ion scales;
- (ii) the plasma dynamics is mainly controlled by few fundamental plasma parameters and the energy injection scale, together with the plasma conditions, is likely much more important than the nature of the energy injection mechanism itself;
- (iii) the main properties of the fluctuations (e.g., compressibility) at ion and sub-ion scales are quite independent of the inertial range, possibly suggesting—together with point (ii)—a certain degree of universality of the kinetic turbulent cascade;
- (iv) electron kinetic processes, intrinsically absent in our DNS, do not seem to play a significant role for the properties here compared at scales larger than the electron characteristic scales, in the particular investigated regime (intermediate ion beta and low electron beta);
- (v) fluctuations at ion and sub-ion scales are likely low-frequency, consistent with a kinetic Alfvén wave-like nature or with quasi-static structures;
- (vi) our 2D DNS results represent a good model for this observed event, compatible with a quasi-2D nature of the turbulent cascade;
- (vii) the inertial-range intermittency is smaller than in the pristine solar wind, consistent with a smaller correlation length of the turbulence due to energy being injected at scales closer to the ion scales;
- (viii) the kurtosis does not saturate at sub-ion scales at the magnetopause, possibly due to a different contribution from coherent structures and/or waves and phase-randomizing structures with respect to the solar wind;
- (ix) the larger cascade rate than the one measured in the ambient magnetosheath suggests that the turbulence we are observing is indeed driven by the KH event rather than preexisting turbulence that the HKI occurs on top of.

In conclusion, we recall that the main fundamental physical parameters allowing us to quantitatively recover many different properties of the turbulence observed by MMS at the magnetopause with a DNS of balanced Alfvénic turbulence are:

1. the ion beta, controlling the scale and shape of the ion-scale break in the magnetic field spectrum and its slope at kinetic scales;
2. the electron beta, affecting the level of the electric field fluctuations at kinetic scales;
3. the amplitude of magnetic fluctuations, determining the energy cascade rate;
4. the injection scales, setting the extent of the MHD inertial range and affecting the intermittency properties.

Additionally, in order to achieve a good agreement simultaneously from the MHD to the sub-ion scales, a very high numerical accuracy is mandatory, in terms of

- (a) a very large number of grid points (here 4096^2), allowing for enough separation between the injection scale, the ion inertial length, and the grid cell size, i.e., a decade of MHD inertial range and a decade at scales smaller than the ion-scale break; and
- (b) a very large number of macro-particles representing the protons (here more than 200 billion in total), allowing for a large statistics and consequently a low numerical noise, with benefits especially for the density and the electric field spectra.

A key difference of our DNS with respect to observations and other simulations investigating the same event (Nakamura et al. 2020) is the initial velocity. The KHI becomes unstable when the velocity shear between the solar wind and the magnetosphere exceeds the Alfvén speed. Hence, the vortex-induced reconnection (VIR) process is controlled by the super-Alfvénic vortex flow (e.g., Nakamura et al. 2011, 2013). As a consequence, the first injection to the VIR turbulence is caused by the strong background plasma flows, that are not included in the present DNS. Although the focus of this study is the stage after the first injection and the consequent development of the turbulent cascade, including realistic injection mechanisms, e.g., the KHI, might provide complementary information.






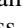


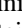


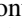
Compressible fluctuations could also be included in the initialization, providing for a better modeling in the inertial range. Despite compressible fluctuations likely playing a role in the large-scale dynamics, there is evidence that the kinetic-scale compressibility is quite independent of its MHD-scale counterpart (e.g., Cerri et al. 2017).

Full kinetic simulations will allow us to extend our modeling of the observed turbulent properties down to electron characteristic scales.

The authors acknowledge valuable discussions with Christopher Chen, William H. Matthaeus, Daniel Verscharen, Riddhi Bandyopadhyay, Leonardo Bianchini, and Christopher James Callow. L.F. and D.B. are supported by the UK Science and Technology Facilities Council (STFC) grants ST/P000622/1 and ST/T00018X/1. J.E.S. is supported by the STFC grant ST/S000364/1. P.H. acknowledges grant 18-08861S of the Czech Science Foundation. T.K.M.N is supported by the Austrian Science Fund (FWF): P32175-N27. This research utilized Queen Mary’s Apocrita HPC facility, supported by QMUL Research-IT (Butcher et al. 2017). We acknowledge PRACE for awarding

us access to resource Cartesius based in the Netherlands at SURFsara through the DECI-13 (Distributed European Computing Initiative) call (project HybTurb3D), and CINECA for the availability of high performance computing resources and support under the IS CRA initiative (grants HP10CQI4XP and HP10B2DRR4) and the program Accordo Quadro INAF-CINECA 2017–2019 (grant C4A26). The LPP involvement for the SCM instrument is supported by CNES and CNRS. The observational data are publicly available through the MMS Science Data Center (<https://lasp.colorado.edu/mms/sdc/public/>).

ORCID iDs

Luca Franci  <https://orcid.org/0000-0002-7419-0527>
 Julia E. Stawarz  <https://orcid.org/0000-0002-5702-5802>
 Emanuele Papini  <https://orcid.org/0000-0002-7969-7415>
 Petr Hellinger  <https://orcid.org/0000-0002-5608-0834>
 Takuma Nakamura  <https://orcid.org/0000-0003-4550-2947>
 David Burgess  <https://orcid.org/0000-0002-8175-9056>
 Simone Landi  <https://orcid.org/0000-0002-1322-8712>
 Andrea Verdini  <https://orcid.org/0000-0003-4380-4837>
 Lorenzo Matteini  <https://orcid.org/0000-0002-6276-7771>
 Robert Ergun  <https://orcid.org/0000-0002-3096-8579>
 Olivier Le Contel  <https://orcid.org/0000-0003-2713-7966>
 Per-Arne Lindqvist  <https://orcid.org/000-0001-5617-976>

References

- Alexandrova, O., Saur, J., Lacombe, C., et al. 2009, *PhRvL*, **103**, 165003
 Andrés, N., Galtier, S., & Sahraoui, F. 2018, *PhRvE*, **97**, 013204
 Arzamasskiy, L., Kunz, M. W., Chandran, B. D. G., & Quataert, E. 2019, *ApJ*, **879**, 53
 Bale, S. D., Kellogg, P. J., Mozer, F. S., Horbury, T. S., & Reme, H. 2005, *PhRvL*, **94**, 215002
 Bandyopadhyay, R., Chasapis, A., Chhiber, R., et al. 2018, *ApJ*, **866**, 106
 Bandyopadhyay, R., Sorriso-Valvo, L., Chasapis, A. R., et al. 2020, *PhRvL*, **124**, 225101
 Belmont, G., & Dhanteur, G. 1989, in *Turbulence and Nonlinear Dynamics in MHD Flows*, ed. M. Meneguzzi, A. Pouquet, & P. Sulem (Elsevier: Amsterdam), 69
 Boldyrev, S., Horaites, K., Xia, Q., & Perez, J. C. 2013, *ApJ*, **777**, 41
 Boldyrev, S., Perez, J. C., Borovsky, J. E., & Podesta, J. J. 2011, *ApJL*, **741**, L19
 Bourouaine, S., Alexandrova, O., Marsch, E., & Maksimovic, M. 2012, *ApJ*, **749**, 102
 Breuillard, H., Matteini, L., Argall, M. R., et al. 2018, *ApJ*, **859**, 127
 Bruno, R. 2019, *E&SS*, **6**, 656
 Bruno, R., & Carbone, V. 2013, *LRSP*, **10**, 2
 Butcher, S., Thomas, K., & Zaleski, L. 2017, *Apocrita - High Performance Computing Cluster for Queen Mary University of London*, Zenodo, doi:10.5281/zenodo.438045
 Cerri, S. S., Franci, L., Califano, F., Landi, S., & Hellinger, P. 2017, *JPIPh*, **83**, 705830202
 Cerri, S. S., Grošelj, D., & Franci, L. 2019, *FrASS*, **6**, 64
 Chandran, B. D. G., Quataert, E., Howes, G. G., Xia, Q., & Pongkitwanichakul, P. 2009, *ApJ*, **707**, 1668
 Chandrasekhar, S. 1961, *Hydrodynamic and Hydromagnetic Stability* (Oxford: Clarendon)
 Chen, C. H. K. 2016, *JPIPh*, **82**, 535820602
 Chen, C. H. K., & Boldyrev, S. 2017, *ApJ*, **842**, 122
 Chen, C. H. K., Boldyrev, S., Xia, Q., & Perez, J. C. 2013, *PhRvL*, **110**, 225002
 Chen, C. H. K., Salem, C. S., Bonnell, J. W., Mozer, F. S., & Bale, S. D. 2012, *PhRvL*, **109**, 035001
 Chen, C. H. K., Sorriso-Valvo, L., Šafránková, J., & Němeček, Z. 2014, *ApJL*, **789**, 12
 Chhiber, R., Chasapis, A., Bandyopadhyay, R., et al. 2018, *JGRA*, **123**, 9941
 Chhiber, R., Usmanov, A. V., Matthaeus, W. H., Parashar, T. N., & Goldstein, M. L. 2019, *ApJS*, **242**, 12
 de Kármán, T., & Howarth, L. 1938, *RSPSA*, **164**, 192
 Ergun, R. E., Tucker, S., Westfall, J., et al. 2016, *SSRv*, **199**, 167
 Eriksson, S., Lavraud, B., Wilder, F. D., et al. 2016a, *GeoRL*, **43**, 5606
 Eriksson, S., Wilder, F. D., Ergun, R. E., et al. 2016b, *PhRvL*, **117**, 015001
 Faganello, M., Califano, F., & Pegoraro, F. 2008a, *PhRvL*, **100**, 015001
 Faganello, M., Califano, F., & Pegoraro, F. 2008b, *PhRvL*, **101**, 105001
 Faganello, M., Califano, F., Pegoraro, F., & Retinò, A. 2014, *EPL*, **107**, 19001
 Fairfield, D. H., Otto, A., Mukai, T., et al. 2000, *JGR*, **105**, 159
 Foullon, C., Farrugia, C. J., Fazakerley, A. N., et al. 2008, *JGRA*, **113**, A11203
 Franci, L., Cerri, S. S., Califano, F., et al. 2017, *ApJL*, **850**, L16
 Franci, L., Hellinger, P., Guarrasi, M., et al. 2018a, *JPhCS*, **1031**, 012002
 Franci, L., Landi, S., Matteini, L., Verdini, A., & Hellinger, P. 2015a, *ApJ*, **812**, 21
 Franci, L., Landi, S., Matteini, L., Verdini, A., & Hellinger, P. 2016, *ApJ*, **833**, 91
 Franci, L., Landi, S., Verdini, A., Matteini, L., & Hellinger, P. 2018b, *ApJ*, **853**, 26
 Franci, L., Verdini, A., Matteini, L., Landi, S., & Hellinger, P. 2015b, *ApJL*, **804**, L39
 Gary, S. P., Chang, O., & Wang, J. 2012, *ApJ*, **755**, 142
 Goldreich, P., & Sridhar, S. 1995, *ApJ*, **438**, 763
 Grošelj, D., Mallet, A., Loureiro, N. F., & Jenko, F. 2018, *PhRvL*, **120**, 105101
 Hadid, L. Z., Sahraoui, F., Galtier, S., & Huang, S. Y. 2018, *PhRvL*, **120**, 055102
 Hasegawa, H., Fujimoto, M., Phan, T. D., et al. 2004, *Natur*, **430**, 755
 Hasegawa, H., Nakamura, T. K. M., Gershman, D., et al. 2020, *JGRA*, **125**, e2019JA027595
 Hellinger, P., Verdini, A., Landi, S., et al. 2020, arXiv:2004.02726
 Hellinger, P., Verdini, A., Landi, S., Franci, L., & Matteini, L. 2018, *ApJL*, **857**, L19
 Karimabadi, H., Roytershteyn, V., Wan, M., et al. 2013, *PhPI*, **20**, 012303
 Kivelson, M. G., & Chen, S.-H. 2013, *GMS*, **90**, 257
 Kiyani, K. H., Chapman, S. C., Khotyaintsev, Y. V., Dunlop, M. W., & Sahraoui, F. 2009, *PhRvL*, **103**, 075006
 Kiyani, K. H., Chapman, S. C., Sahraoui, F., et al. 2013, *ApJ*, **763**, 10
 Kiyani, K. H., Osman, K. T., & Chapman, S. C. 2015, *RSPTA*, **373**, 20140155
 Kobayashi, S., Sahraoui, F., Passot, T., et al. 2017, *ApJ*, **839**, 122
 Le Contel, O., Leroy, P., Roux, A., et al. 2016, *SSRv*, **199**, 257
 Li, W., André, M., Khotyaintsev, Y. V., et al. 2016, *GeoRL*, **43**, 5635
 Lindqvist, P.-A., Olsson, G., Torbert, R. B., et al. 2016, *SSRv*, **199**, 137
 MacBride, B. T., Forman, M. A., & Smith, C. W. 2005, in *ESA Special Publication 592, Solar Wind 11/SOHO 16*, Connecting Sun and Heliosphere, ed. B. Fleck, T. H. Zurbuchen, & H. Lacoste (Les Ulis: EDP Sciences), 613
 Macek, W. M., Krasniška, A., Silveira, M. V. D., et al. 2018, *ApJL*, **864**, L29
 Matteini, L., Alexandrova, O., Chen, C. H. K., & Lacombe, C. 2017, *MNRAS*, **466**, 945
 Matthaeus, W. H., Parashar, T. N., Wan, M., & Wu, P. 2016, *ApJ*, **827**, L7
 Matthaeus, W. H., & Velli, M. 2011, *SSRv*, **160**, 145
 Matthaeus, W. H., Wan, M., Servidio, S., et al. 2015, *RSPTA*, **373**, 20140154
 Mishin, V. V., & Morozov, A. G. 1983, *P&SS*, **31**, 821
 Miura, A., & Pritchett, P. L. 1982, *JGR*, **87**, 7431
 Nakamura, T., Stawarz, J., Hasegawa, H., et al. 2020, *JGRA*, **125**, e2019JA027515
 Nakamura, T. K. M. 2020, in *The Earth's Low-latitude Boundary Layer*, ed. R. Maggiolo et al. (New York: Wiley)
 Nakamura, T. K. M., Daughton, W., Karimabadi, H., & Eriksson, S. 2013, *JGRA*, **118**, 5742
 Nakamura, T. K. M., Eriksson, S., Hasegawa, H., et al. 2017a, *JGRA*, **122**, 11505
 Nakamura, T. K. M., Hasegawa, H., Daughton, W., et al. 2017b, *NatCo*, **8**, 1582
 Nakamura, T. K. M., Hasegawa, H., Shinohara, I., & Fujimoto, M. 2011, *JGRA*, **116**, A03227
 Papini, E., Franci, L., Landi, S., et al. 2019, *ApJ*, **870**, 52
 Parashar, T. N., Salem, C., Wicks, R. T., et al. 2015, *JPIPh*, **81**, 905810513
 Passot, T., & Sulem, P.-L. 2015, *ApJL*, **812**, L37
 Passot, T., Sulem, P. L., & Tassi, E. 2018, *PhPI*, **25**, 042107
 Phan, T. D., Eastwood, J. P., Shay, M. A., et al. 2018, *Natur*, **557**, 202
 Podesta, J. J., Roberts, D. A., & Goldstein, M. L. 2007, *ApJ*, **664**, 543
 Politano, H., & Pouquet, A. 1998, *PhRvE*, **57**, R21
 Pollock, C., Moore, T., Jacques, A., et al. 2016, *SSRv*, **199**, 331
 Pollock, C. J., Burch, J. L., Chasapis, A., et al. 2018, *JASTP*, **177**, 84
 Pucci, F., Servidio, S., Sorriso-Valvo, L., et al. 2017, *ApJ*, **841**, 60
 Roberts, O. W., Toledo-Redondo, S., Perrone, D., et al. 2018, *GeoRL*, **45**, 7974
 Roytershteyn, V., Boldyrev, S., Delzanno, G. L., et al. 2019, *ApJ*, **870**, 103
 Russell, C. T., Anderson, B. J., Baumjohann, W., et al. 2016, *SSRv*, **199**, 189

- Šafránková, J., Němeček, Z., Němec, F., et al. 2015, *ApJ*, **803**, 107
- Šafránková, J., Němeček, Z., Němec, F., et al. 2016, *ApJ*, **825**, 121
- Sahraoui, F., Goldstein, M. L., Belmont, G., Canu, P., & Rezeau, L. 2010, *PhRvL*, **105**, 131101
- Sahraoui, F., Goldstein, M. L., Robert, P., & Khotyaintsev, Y. V. 2009, *PhRvL*, **102**, 231102
- Servidio, S., Valentini, F., Perrone, D., et al. 2015, *JPIPh*, **81**, 325810107
- Sharma Pyakurel, P., Shay, M. A., Phan, T. D., et al. 2019, *PhPI*, **26**, 082307
- Sorriso-Valvo, L., Catapano, F., Retinò, A., et al. 2019, *PhRvL*, **122**, 035102
- Sorriso-Valvo, L., Marino, R., Carbone, V., et al. 2007, *PhRvL*, **99**, 115001
- Stawarz, J. E., Eastwood, J. P., Phan, T. D., et al. 2019, *ApJL*, **877**, L37
- Stawarz, J. E., Eriksson, S., Wilder, F. D., et al. 2016, *JGR*, **121**, 11
- Sturmer, A. P., Eriksson, S., Nakamura, T., et al. 2018, *JGR*, **123**, 1305
- Taylor, G. I. 1938, *RSPSA*, **164**, 476
- TenBarge, J. M., & Howes, G. G. 2013, *ApJL*, **771**, L27
- Told, D., Jenko, F., TenBarge, J. M., Howes, G. G., & Hammett, G. W. 2015, *PhRvL*, **115**, 025003
- Valentini, F., Váscónez, C. L., Pezzi, O., et al. 2017, *A&A*, **599**, A8
- Váscónez, C. L., Valentini, F., Camporeale, E., & Veltri, P. 2014, *PhPI*, **21**, 112107
- Vasquez, B. J., Markovskii, S. A., & Chandran, B. D. G. 2014, *ApJ*, **788**, 178
- Verdini, A., Grappin, R., Hellinger, P., Landi, S., & Müller, W. C. 2015, *ApJ*, **804**, 119
- Vernisse, Y., Lavraud, B., Eriksson, S., et al. 2016, *JGRA*, **121**, 9926
- Verscharen, D., Klein, K. G., & Maruca, B. A. 2019, *LRSP*, **16**, 5
- Vörös, Z., Baumjohann, W., Nakamura, R., Volwerk, M., & Runov, A. 2006, *SSRv*, **122**, 301
- Wan, M., Matthaeus, W. H., Roytershteyn, V., et al. 2015, *PhRvL*, **114**, 175002
- Wilder, F. D., Ergun, R. E., Schwartz, S. J., et al. 2016, *GeoRL*, **43**, 8859
- Wu, P., Perri, S., Osman, K., et al. 2013, *ApJL*, **763**, 30
- Zhdankin, V., Uzdensky, D. A., Werner, G. R., & Begelman, M. C. 2019, *PhRvL*, **122**, 055101
- Zimbaro, G., Greco, A., Sorriso-Valvo, L., et al. 2010, *SSRv*, **156**, 89